POLITECNICO MILANO 1863

Post-Print

When citing this work, cite the original published paper.

Permanent link to this version
http://hdl.handle.net/11311/1131526

Dynamic Mode Decomposition Analysis of Plasma Aeroelastic Control of Airfoils in Cascade

P. Neumann[a,1,*], V. B. C. de Almeida[a,1,**], V. Motta[b,2,**], L. Malzacher[a,1], D. Peitsch[a,3], G. Quaranta[c,3]

[a]*Technische Universität Berlin, Institute of Aeronautics and Astronautics, Chair for Aero Engines, Marchstraße 12-14 10587 Berlin, Germany*
[b]*GE Renewable Energy, Advanced Technology & Sciences, Franklinstraße 14, 10587 Berlin, Germany*
[c]*Politecnico di Milano, Department of Aerospace Sciences and Technology, via La Masa 34, 20156 Milano, Italy*

Abstract

A dynamic mode decomposition (DMD) is carried out for the flow field in a compressor cascade with plasma actuators employed for aeroelastic control. Numerical assessments performed in previous works have shown that alternate triggering of pressure side/suction side actuators installed at the trailing edge of the blades can effectively reduce vibratory loads and enlarge the flutter boundaries of a linear compressor cascade. With the twofold aim of obtaining an in-depth understanding of the flow physics associated to plasma actuation and ultimately developing an optimized control law for the actuators, the dominant structures of the pressure field are extracted via a dynamic mode decomposition. The decomposition is conducted on the actuated and non-actuated pressure fields at several inter blade phase angles. The fundamental effects of plasma actuations on the flow field, and in turn on the blade loading, are identified and discussed. The procedure allows to get an useful picture of the main fluid mechanic phenomena associated to plasma aeroelastic control on turbomachinery blades. Additionally, the DMD spectrum and its coherence are analysed, yielding a wider energetic spread over high-order modes for the plasma-actuated case, in comparison to the clean cascade.

Keywords: Reduced Order Modeling, Dynamic Mode Decomposition, Plasma Actuation, Aeroelastic Control.

1. Introduction

The demand for lighter and more efficient aero engines is continuously growing. To face these challenges, compressors with increasingly larger pressure ratio per stage have been

---

[*]Principal corresponding author
[**]Corresponding author
Email addresses: `p.neumann@tu-berlin.de` (P. Neumann), `victor.bicalho@ilr.tu-berlin.de` (V. B. C. de Almeida), `valentina.motta@ge.com` (V. Motta)
[1]PhD fellow
[2]Lead engineer, system dynamics and optimization
[3]Full professor

designed. Natural consequences of these solutions are increasing risks of fatigue and flutter phenomena on compressor blades. Degradations in aerodynamic and aerostructural response are also encountered on engines with pressure gain combustion integration (such as pulsed or rotating detonation), currently under study within the Collaborative Research Center 1029 of Technische Universität Berlin[4]. Several solutions have been proposed to control flow separation and minimize pressure losses arising on these novel configurations [1, 2, 3, 4, 5, 6]. Among the conceived approaches, plasma actuators seem to be very promising, thanks to their lightness and to their almost negligible intrusiveness in the flow [7]. Whereas the control of the aerodynamic performance on heavily loaded blades has been widely investigated, the aeroelastic feasibility problems of these new designs have not yet been thoroughly pursued. In previous works, the authors showed numerically that plasma actuators may be successfully employed as virtual control surfaces to reduce vibration [8, 9] and to enlarge the flutter boundaries [10, 11] on a linear compressor cascade.

Even though this work does not deal with the practical implementation of plasma actuators for aeroelastic control of turbomachinery blades, it is worth further discussing the topic. The implementation of an active control with on-blade actuators is a challenging task, especially for rotating blades. For instance, mechanical actuators -- featuring moving parts -- are likely to fail in a very short time, due to large centrifugal forces and high temperatures. Moreover, the implementation of such devices onto turbomachinery blades would require disruptive modifications in the structural design, with enhanced risks of structural failures due to stress concentrations and increased vibrations. Similarly, flow blowing/suction requires the realization of holes on the blade surface, with consequent flow disturbances and increase of local stresses. Potential drawbacks of other active control devices are discussed in [11] and are not reported here for brevity purposes.

The particular suitability of plasma actuators for aero engine blades lies in their lightness,

---

[4]Substantial efficiency increase in gas turbines through direct use of coupled unsteady combustion and flow dynamics, https://www.sfb1029.tu-berlin.de/menue/sfb_1029/parameter/en/.

the absence of moving parts, and the nearly null intrusiveness in the flow field, with a thickness of about 10^{-4}m [7]. For closed-loop control, one possible path is the development of microcontrollers and microgenerators, small enough to be located in targeted hollows of the rotating system, which is currently pursued by the authors in cooperation with the university of Salento. The installation of plasma actuators on rotor blades requires the actuation energy to be transferred from the fixed to the rotating frame of reference. High quality standards are required for this transmission, to minimize signal distortions and maximize the actuation effectiveness. Moreover, the necessary actuation energy needs to be transferred from the stationary to the rotating frame of reference with an high demand of transmission quality. Especially low noise and very low time lags have to be ensured. One possible solution for this is the use of devices like ROTRANS, which have already been employed by [12, 13]. In this case, the transmission of signals between stationary and rotating frames of reference is achieved with the help of a liquid metal medium.

It is also worth noting that state-of-the-art plasma actuators are found to be effective even in transonic flows -- which may be encountered also in aero engine compressors. In particular, Saddoughi et al. [14] showed that plasma actuators are capable to act effectively on the flow field also in transonic flow conditions. Improvements in the stall margin up to 4% in a transonic compressor stage were achieved in [14].

With the ultimate aim of designing optimal open- and closed-loop control architectures, it is necessary to develop an appropriate reduced order model (ROM). In this work -- carried out within the Collaborative Research Centre 1029 of TU Berlin -- a dynamic mode decomposition (DMD), first proposed in [15], is developed for the clean -- i.e. non-actuated -- and the plasma-equipped cascade, capable to reproduce accurately the unsteady behaviour of the blades. The decomposition is applied on the flow field issued by the computational fluid dynamic (CFD) assessments detailed in [8, 10, 9, 11], in the actuated and non-actuated case. The capability of the proposed ROM in reproducing the most relevant flow dynamics is highlighted. A further advantage of the dynamic mode decomposition is the possibility of getting an insight into the flow physics associated to this novel concept of active aeroelastic control. This paper is structured as follows. The

numerical model and selected CFD results are presented in section 2. A brief overview on the theoretical aspects and on the formulation of the dynamic mode decomposition is provided in section 3. The results achieved by applying the DMD on the clean and actuated cascade are reported in section 4, where the spatial modes, spectrum, coherence and far-field assessments are presented. Concluding remarks are given in section 5.

2. Computational fluid dynamic assessments

2.1. Baseline flow with and without plasma actuation

The DMD is applied on the numerically simulated flow field of a linear compressor cascade. The cascade resembles the aeroelastic test rig of the Chair of Aero Engines at TU Berlin [16]. The two-dimensional cascade features NACA 65 series airfoils, with a chord length of 0.15 m and a pitch-to-chord ratio of 0.75. Experimental tests showed that the flow can be considered as two-dimensional, for the investigated range of freestream conditions and for the small amplitude blade oscillations taken under consideration [16]. Thus, a 2D CFD-model is applied.
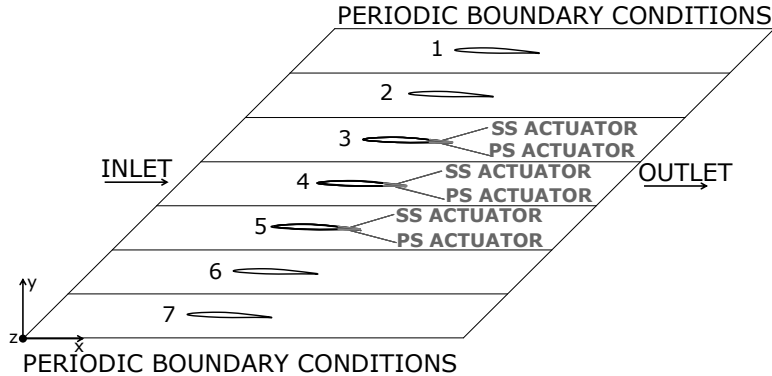

Figure 1: Sketch of the computational geometry for the linear cascade

The cascade is modelled with 7 blades and periodic boundary conditions on the top and on the bottom, as shown in figure 1. At the inlet, the freestream velocity U is imposed, whereas at the outlet a pressure value of 101,325 Pa is defined. For the actuated case, plasma actuators are modelled on the rear side of the three central blades, on the suction side (SS) and pressure side (PS). For the numerical simulations, the finite volume solver Ansys CFX is employed. The advection terms are solved with a high resolution scheme,

whereas the second order backward scheme is applied for the transient terms. The flow is assumed as fully turbulent, and the system of RANS equations is closed with the SST k-ω turbulence model. It's worth remarking that the same numerical approach was used by Keehrti et al. [17] to perform numerical simulations on a linear compressor cascade with airfoils oscillating in traveling wave mode. Therefore, the selected numerical model is regarded as appropriate also for the present work. More details on the choice of the numerical model for the present computations are reported in [11].

A multi-block grid, consisting of $\approx 600,000$ quadrilateral elements, is realized to perform the computations. The mesh is designed with a refinement at the blade surface walls resulting in a y^+ value close to 1. The incompressible flow simulations are conducted with chord-based Reynolds numbers of ≈ 195000 and ≈ 350000. The temperature is set to 20°C and the reference pressure to 101,325 Pa.

The plasma actuators are implemented on the rear side of the blades on the SS and PS as 10 mm wide and 0.1 mm thick actuation areas, see figure 2. Consistently with [18, 19], the plasma actuation is implemented as a body force, directed against the freestream direction. Steady simulations showed a different effectiveness of the suction side actuation and the pressure side actuation [8]. That is, to obtain quantitatively comparable effects in the air loads (with opposite sign), a larger body force must be applied on the SS. Therefore, the SS actuation force (per unit length) is set to 450 mN/m and the PS actuation force to 225 mN/m. Notice that the body forces are still compliant with modern plasma actuators, see e.g. [20]. Actuating against the freestream causes the development of low-speed recirculating flow areas. This yields an increase in static pressure, which is maximum in the actuator area and which -- for subsonic flows -- propagates upstream up to the leading edge. Therefore, PS actuation will yield effects comparable to those of a flap-like device deflected downward. That is, lift and nose-down pitching moment will be increased [21, 9]. Conversely, SS actuation will provide effects comparable to those of a trailing edge spoiler, i.e., lift and nose-down pitching moment will be decreased [21, 9].
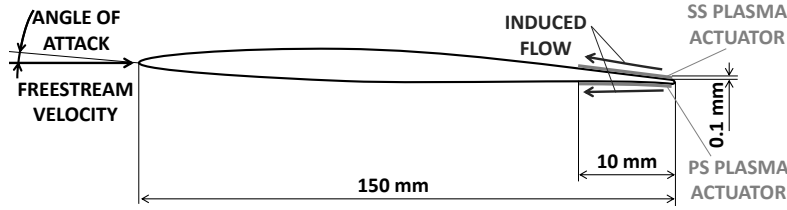
Figure 2: Sketch of the blade section with the plasma actuators.

The reliability of the numerical computations has been shown in [8, 10, 9, 11], where space and time convergence studies, as well as comparison with experimental data, are reported. The reader is referred to these works for more detailed information on this regard.

2.2. Reference numerical results with and without plasma actuation

The unsteady flow simulations are carried out for several travelling wave modes. A travelling wave mode, first introduced by Lane [22], describes the specific blade motion of tuned rotors. According to the travelling wave mode formulation, blades oscillate with the same shape, frequency f_{osc} and amplitude, but with a constant and uniform phase shift between two adjacent blades, referred to as Inter Blade Phase Angle (IBPA). Each single-blade structural eigenmode generates, in combination with the airloads, a specific set of travelling wave modes. Travelling wave pitch modes (about the mid-chord) are considered in this work. Indeed, experimental tests carried out on the cascade under consideration have highlighted that the purely torsional pitch mode is the most unstable, whereas the bending mode is far from the instability threshold [23]. Specifically, the blade mean angle of attack and the oscillation amplitude are set to 2° and 1°, respectively. The reduced frequency based on the semi-chord is $k = \pi f_{osc} c/U = 0.4597$, where c is the blade chord and U the freestream velocity. This specific value of the reduced frequency has been selected because it is the one at which flutter was detected experimentally on the considered cascade [23].

The dynamic actuation is set to maximize the aeroelastic stability, i.e. the net flow of energy transferred from the blade to the flow. To this aim, and consistently with the recommendations of [24], SS plasma is triggered during the upstroke phase -- nose moving upward -- of the pitching cycle. Conversely, PS plasma is triggered during the downstroke phase. Figure 3 sketches the triggering of PS and SS actuation relative to the time history

6

of the moment coefficient and to the blade motion. The light grey area highlights the operating window of the SS actuation. On the other hand, the dark grey area shows the operating window of the PS actuation.
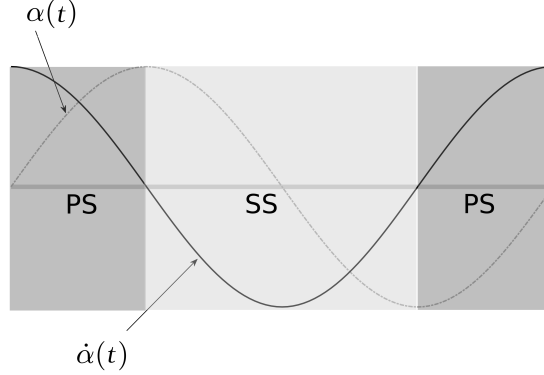

Figure 3: Sketch of PS and SS actuation triggering with respect to the blade motion $\alpha(t)$ and of its time derivative $\dot{\alpha}(t)$.

Figure 4 (top) shows TE details of the velocity magnitude field during an oscillation cycle of a travelling wave mode simulation. The velocity is made dimensionless with the freestream velocity. The central blade of the cascade is displayed. PS actuation generates the expected recirculating flow areas during the downstroke phase, with a consequent increase in the blade loading relative to the clean counterpart. The opposite occurs during the upstroke phase [10, 11]. The oscillatory loads obtained with and without actuation are displayed in Fig. 4 (bottom left and bottom middle). The reduction in the unsteady lift and moment peaks enabled by alternate PS/SS actuation is clearly visible. Beneficial effects on the blade aeroelastic stability provided by unsteady plasma actuation are also obtained. Figure 4 (bottom) shows the non-dimensional aerodynamic work Ξ, versus the IBPA, with and without actuation. As in [10, 11], $\Xi = -W_{\mathrm{aero}}/\pi\, q\, c^2\, \bar{\alpha}^2$, where $q = 0.5\,\rho\, U^2$ is the dynamic pressure with fluid density ρ, and $\bar{\alpha} = 1°$ the harmonic oscillation amplitude. W_{aero} is the aerodynamic work on the blade.

With the ultimate aim of developing an actuation law which maximizes the effectiveness of the control for the different operating regimes of the compressor, large scale optimization studies need to be performed. Indeed, an effective feed-forward or feed-back architecture has to operate under different flow velocities, vibration amplitudes, measurement uncertainties, dead times, coupled modes, switch of control law in dependency of the most urgent problem
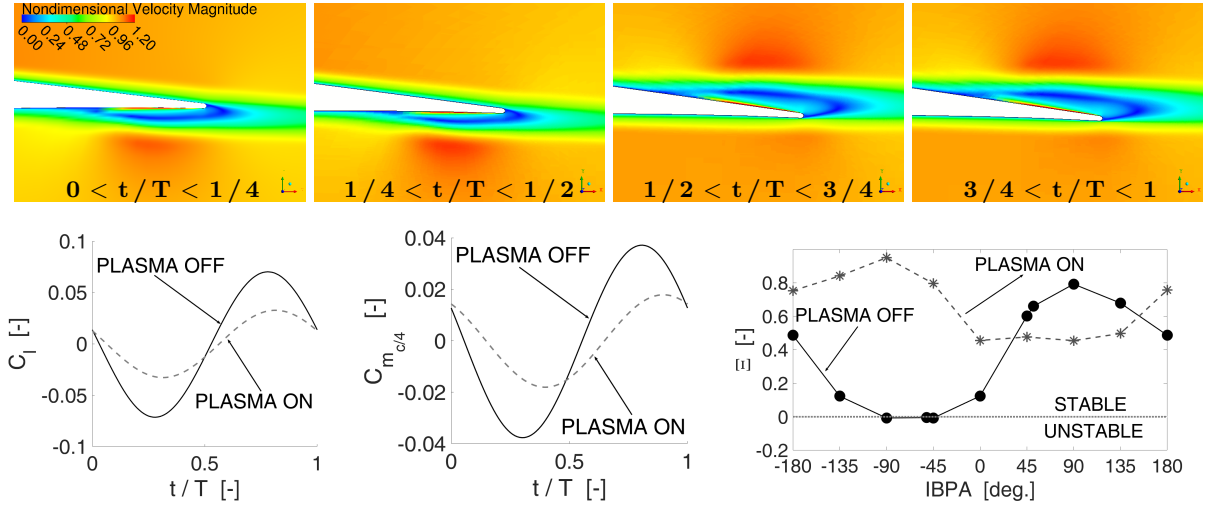
7

Figure 4: Top: TE detail of velocity magnitude, normalized by the freestream velocity, over the oscillation cycle; plasma actuation on. Bottom left and bottom middle: time history of lift and moment coefficient oscillations without and with actuation. Bottom right: aerodynamic damping versus IBPA with and without plasma. Re $\approx 1.9 \times 10^5$; IBPA = -51.43 °; $\alpha = 2° + \sin\left(2\pi f_{osc} t + 4 \times IBPA\right)$; $f_{osc} = 19.17$ Hz, T = $1/f_{osc}$; PS body force: 225 mN/m; SS body force: 450 mN/m.

(stability or forced vibrations).

However, numerous simulations need to be performed for every flow and vibration case during this optimization. Furthermore, the implementation of an aeroelastic control for a 3D geometry is planned in the future. Therefore, a tremendous rise of computational burden would occur when performing CFD-based optimization studies of actuation laws. Within this framework it appears useful to build up a reduced order model which allows to evaluate rapidly the performance of the aeroelastic control system, whilst reproducing correctly the dominant physical phenomena of the flow field.

In this work the dynamic mode decomposition will be applied to the pressure fields. This flow variable is chosen because it leads directly to the aerodynamic loads, which are further needed to calculate the aeroelastic behaviour. It will be shown that the model is capable to retain the most important flow dynamics and can therefore be used to compute accurately and rapidly the unsteady airloads on the clean and actuated cascade. Moreover, the dynamic mode decomposition allows to have an useful picture of the physical phenomena associated to the alternate PS/SS plasma actuation first proposed by the

authors in [8, 9, 10, 11].

3. Overview on the dynamic mode decomposition

The proper orthogonal decomposition (POD) has been and still is widely used to extract the main structures of complex flows, see e.g. [25, 26, 27]. Specifically, spatially orthogonal structures are extracted, by computing the correlation matrix of flow field snapshots. The coherent structures, ranked according to the energy content, can be extracted by diagonalizing the computed correlation matrix. However, the spatial POD modes are not temporarily independent and each of them is often contaminated by other uncorrelated structures. Due to this impurity, especially the higher order modes may lack physical meaningfulness.

In order to overcome these limitations, Schmid [15] and Rowley [28] introduced the dynamic mode decomposition (DMD), in which the dynamic modes are extracted by applying the Koopman operator to the flow snapshots, without recurring to any statistical indicator. Compared to the POD, the DMD modes aim at temporal -- yet not spatial -- orthogonality. Therefore the DMD allows to identify correctly the dynamic evolution of the system, as the misleading coupling of temporal modes is avoided. The DMD is based on the fitting of the data sequence with a high order polynomial, which is meant to approximate the temporal evolution of the system. The fitting polynomial is an finite dimension space containing also the dynamics of the dataset, i.e. of the flow. It is proved that the eigenfunctions of a properly selected subspace of the fitting polynomial are a realistic representation of the dynamic response of the system under consideration [28]. Starting from the seminal works of [15, 28], the DMD has been effectively applied to several problems, including e.g. the flow past cylinders [26], the near-wake flow of a Gurney flap [29], turbulent cavity flows [30] or shallow flows [31]. A brief overview on the DMD algorithm is given hereinafter. For more details, please refer to [15, 28].

The flow field -- e.g. velocity, vorticity, pressure -- retrieved with numerical computations or particle image velocimetry surveys can be collected into a matrix containing temporally equidistant snapshots. This matrix can be written as $\boldsymbol{V}_1^N = \{\boldsymbol{v}_1, \boldsymbol{v}_2, ..., \boldsymbol{v}_N\}^{M \times N}$, being N the number of recorded time steps and M the number of sample points within a snapshot.

If the collected ensemble is large enough to approach the system dynamics asymptotically, it is possible to employ a constant mapping $\boldsymbol{A}$ relating one snapshot (j) to the following one $(j+1)$. Therefore it is possible to write:

$$\boldsymbol{v}_{j+1} = \boldsymbol{A}\boldsymbol{v}_j, \tag{1}$$

where $\boldsymbol{A}$ is the same for $j = 1, 2, ..., N-1$. The eigenvalues of $\boldsymbol{A}$ can be computed by defining the Krylov sequence and by performing an Arnoldi iteration on the resulting matrix. By adopting this approach, the matrix $\boldsymbol{V}_1^{N-1}$ which subtracts the last snapshot from the original data matrix can be expressed as $\boldsymbol{V}_1^{N-1} = \{\boldsymbol{v}_1, \boldsymbol{A}\boldsymbol{v}_1, \boldsymbol{A}^2\boldsymbol{v}_1, ..., \boldsymbol{A}^{N-2}\boldsymbol{v}_1\}$. Therefore one gets:

$$\boldsymbol{A}\boldsymbol{V}_1^{N-1} = \boldsymbol{V}_2^N, \tag{2}$$

being $\boldsymbol{V}_2^N = \{\boldsymbol{v}_2, \boldsymbol{v}_3, ..., \boldsymbol{v}_N\}$. The matrix $\boldsymbol{A}$ maps the flow at the time step j into the flow at the time step $j+1$. The operation of the matrix $\boldsymbol{A}$ can be seen also as shifting temporally the flow field at the time step j to the time step $j+1$. Ultimately, $\boldsymbol{A}$ can be interpreted as the state transition matrix of a generic dynamic system. Consistently, the eigenvalues of the mapping matrix $\boldsymbol{A}$ will provide information on the dynamic behaviour of the flow field. The matrix $\boldsymbol{A}$ is replaced by employing the lower-dimensional, approximating matrix $\boldsymbol{S}$. This allows the numerical calculation of the system dynamics, since the size of matrix $\boldsymbol{A}$ (namely $M \times M$) would be computationally prohibitive. Specifically equation (2) is expressed as:

$$\boldsymbol{A}\boldsymbol{V}_1^{N-1} = \boldsymbol{V}_2^N = \boldsymbol{V}_1^{N-1}\boldsymbol{S} + \boldsymbol{r}e_{N-1}^{\mathrm{T}} \approx \boldsymbol{V}_1^{N-1}\boldsymbol{S}, \tag{3}$$

being $\boldsymbol{S}$ a companion approximating matrix and $\boldsymbol{r}$ the residual [15]. The matrix $\boldsymbol{S}$ is computed by performing a least squares minimization of equation (3) with respect to $\boldsymbol{r}$. The eigenfunctions of $\boldsymbol{S}$ are known to approximate the counterparts of the reference matrix $\boldsymbol{A}$. As a consequence, performing a global stability analysis on the matrix $\boldsymbol{S}$ provides an approximation of the actual flow dynamics contained in $\boldsymbol{A}$. Instead of directly working with $\boldsymbol{S}$, a similarity transformation is performed, to obtain $\tilde{\boldsymbol{S}} = \boldsymbol{U}^H\boldsymbol{A}\boldsymbol{U}$, being $\boldsymbol{U}$ the

left singular vectors of $\boldsymbol{V}_1^{N-1}$, obtained through a singular value decomposition. This procedure enhances the robustness of the computation (see [15]). The jth equation of eigenvalue problem for $\tilde{\boldsymbol{S}}$ reads:

$$\tilde{\boldsymbol{S}}\boldsymbol{y}_j = \mu_j\boldsymbol{y}_j, \tag{4}$$

where $\mu_j \in \mathbb{C}$ approximates the eigenvalues of $\boldsymbol{A}$. The eigenvalues corresponding to the continuous dynamical system (ω_j) can be retrieved by computing the logarithmic decrement associated to μ_j, i.e. $\omega_j = \log\mu_j/\Delta t = \Re(\omega_j) + \text{i}\,\Im(\omega_j) = \omega_j^r + \text{i}\,\omega_j^i$ -- being Δt the time step. The real part of ω_j sets the time rate of growth/decay for the jth mode of the flow quantity under consideration. On the other hand, the imaginary part of ω_j quantifies the frequency of the jth mode under consideration. The jth spatial mode is computed as $\Phi_j = \boldsymbol{V}_1^{N-1}\boldsymbol{y}_j$. That is, based on equation (3), the modes are retrieved by projecting the flow field $\boldsymbol{V}_1^{N-1}$ onto the eigenvectors of $\tilde{\boldsymbol{S}}$. As a result, the flow field reconstructed with isolated dynamic modes can be expressed as:

$$\boldsymbol{V}_1^{N-1}(x, y, t) = \sum_{j=1}^{N-1} \Phi_j(x, y)\, a_j(t)\, b_j, \tag{5}$$

where a_j takes the form

$$a_j = \text{e}^{(\omega_j^r + \text{i}\,\omega_j^i)\,t}, \tag{6}$$

and b_j stands for the initial amplitude of each mode Φ_j. By projecting each DMD spatial mode Φ_j onto the array $\boldsymbol{U}$, and subsequently taking its norm, a modal coherence metric is obtained, depicting the importance of large-scale energetic structures in the flow. This value, for each mode j, is computed as $||\Phi_j^T\,\boldsymbol{U}||$, as in [32].

In this work, the DMD is applied to the pressure field of the central passage of the aforementioned compressor cascade, sketched in figure 1, with and without plasma actuators. The results are discussed in the following section.

4. Results

The DMD is computed for the pressure field in the central passage of the cascade. Four different IBPAs are taken under consideration, namely, -90°, -51°, -45° and +51°. These specific negative values are considered as the cascade is aeroelastically unstable for IBPAs in the range $\approx$[-120°, -30°]. One additional positive IBPA is considered, for completeness. It is worth remarking that, according to the convention adopted in this work, negative IBPAs indicate a pressure wave travelling from the pressure side of a blade to the suction side of the adjacent blade. Conversely, for positive IBPAs, the pressure wave travels from the suction side of a blade to the pressure side of the neighboring blade. The clean configuration, as well as the plasma-equipped blade actuated to the sketch of figure 3, are considered. It is useful to recall that the DMD is performed for the blades oscillating about the mid-chord, according to a travelling wave pitch mode. The mean angle of attack, the oscillation amplitude and the semi-chord reduced frequency are 2°, 1° and 0.4597, respectively. The chord-based Reynolds number is $\approx$195,000.

Initially, the sensibility of the DMD to data quality has been assessed. Three main features have been analysed: (i) choice of first snapshot, (ii) sampling rate of snapshots and (iii) total number of snapshots: (i) The DMD modes and the residual r of the QR decomposition (see equation 3) do not change significantly for different first snapshots. (ii) The DMD modes and the residual are less sensitive to the sampling rate of snapshots than to the number of snapshots in our case. The results show similar residuals starting between 25 to 50 samples per oscillation cycle. Finally, 100 snapshots per cycle are taken, securing the independency of the DMD modes in regard to the sampling rate. (iii) The residual of the QR decomposition falls two orders of magnitude when increasing the total number of oscillation cycles from 1 to 2 (conversely total number of snapshots from 100 to 200). Further increase in the total number of cycles (snapshots) yields only marginal change in the QR residual as well in the DMD modes.

The selected number of snapshots includes two blade oscillation cycles, with a good periodic convergence already achieved in the first oscillation cycle. Therefore, for low frequencies two modes occur with very similar frequency, with one mode having a much higher coherence. As discussed in more detail later on, just the one mode with higher coherence is considered as significant for a possible flow field reconstruction. Therefore just these significant DMD modes are adressed and presented in this subchapter. These DMD modes are further numbered in ascending frequency, starting with mode 1 having a frequency of 0 Hz. The results show that the frequencies of low-order modes correspond to harmonics of the fundamental blade oscillation frequency. The first mode represents the mean pressure field and its frequency is therefore zero. The second mode frequency is 19.17 Hz, which is the blade oscillation frequency. Mode 3 has a frequency of 38.34 Hz, which is indeed twice the blade oscillation frequency. Mode 4 has a frequency of 58.51 Hz, i.e., three times the blade oscillation frequency. Further, all calculated modes up to mode 20 match integer multiples of the blade oscillation frequency. This demonstrates that the most important periodic phenomena in the system are indeed the ones related to the oscillation/actuation frequency, which are correctly and precisely captured by the DMD. This is not always the case for complex problems where relevant flow dynamics at frequencies other than the disturbance inputs occur and also play an important role, see e.g. [27].

The pressure modes for an IBPA = +51° for the clean configuration are depicted in figure 5. For an IBPA of -51° the pressure modes for the clean and actuated case are shown in figures 6 and 7. Only the real part of each mode is shown in the present work, being the modes ordered by frequency. The first, zero-frequency DMD mode in figure 5(a) represents the mean pressure field. It differs for clean and actuated cases, but it is rather indifferent to the IBPA. The effects of the actuation are clearly visible in terms of pressure distribution at the trailing edge (compare modes in figures 6(a) and 7(a), for example). In comparison with the non-actuated case, low-pressure areas close to the actuators with accompanying upstream high-pressure areas are seen. The pressure mode belonging to the fundamental oscillation frequency f_{osc} in figures 5(b) and 6(b) shows the pressure

distribution corresponding to the travelling wave modes with an IBPA $= +51°$ and an IBPA $= -51°$. As expected, the different phase shift of the blade oscillation of adjacent blades for different IBPAs also generates different unsteady pressure variation, clearly seen in the DMD modes.
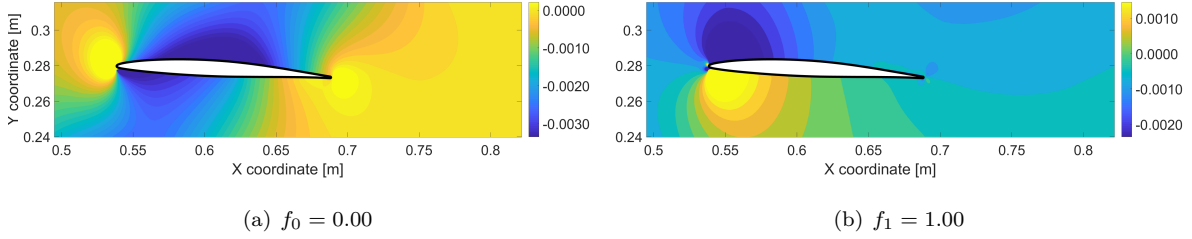

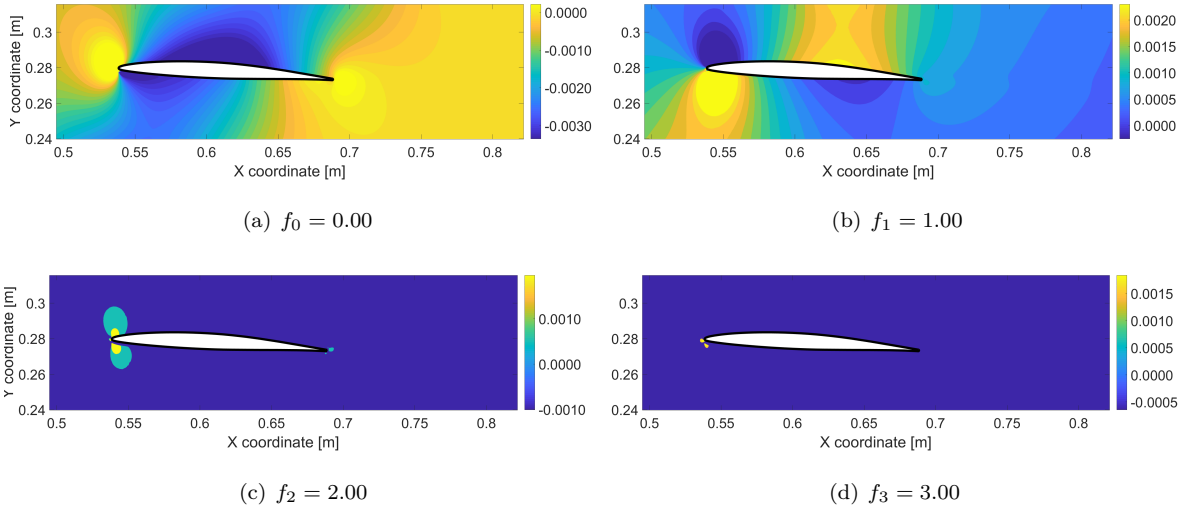(a) $f_0 = 0.00$ (b) $f_1 = 1.00$

Figure 5: DMD modes of pressure field with different normalized frequencys ($f_n = \frac{f}{f_{osc}}$ with $f_{osc} = 19.17\,\mathrm{Hz}$; $n = 0, 1, 2, 3...$) on the central blade with plasma off; IBPA $= 51°$.

(a) $f_0 = 0.00$ (b) $f_1 = 1.00$

(c) $f_2 = 2.00$ (d) $f_3 = 3.00$

Figure 6: DMD modes of pressure field with different normalized frequencys ($f_n = \frac{f}{f_{osc}}$ with $f_{osc} = 19.17\mathrm{Hz}$; $n = 0, 1, 2, 3...$) on the central blade with plasma off; IBPA = -51°.

The change in the DMD modes for the actuated cases with respect to the clean case is most pronounced near the actuation area but is also seen in the overall pressure distribution, including the features of the travelling wave. The actuation influences the pressure field not only on the blade itself, but also on adjacent blades. Higher-order modes also depicted in figure 7 show that most of the unsteady dynamics in the actuated case indeed takes place close to the actuators. The actuation leads to a significant increase in the pressure
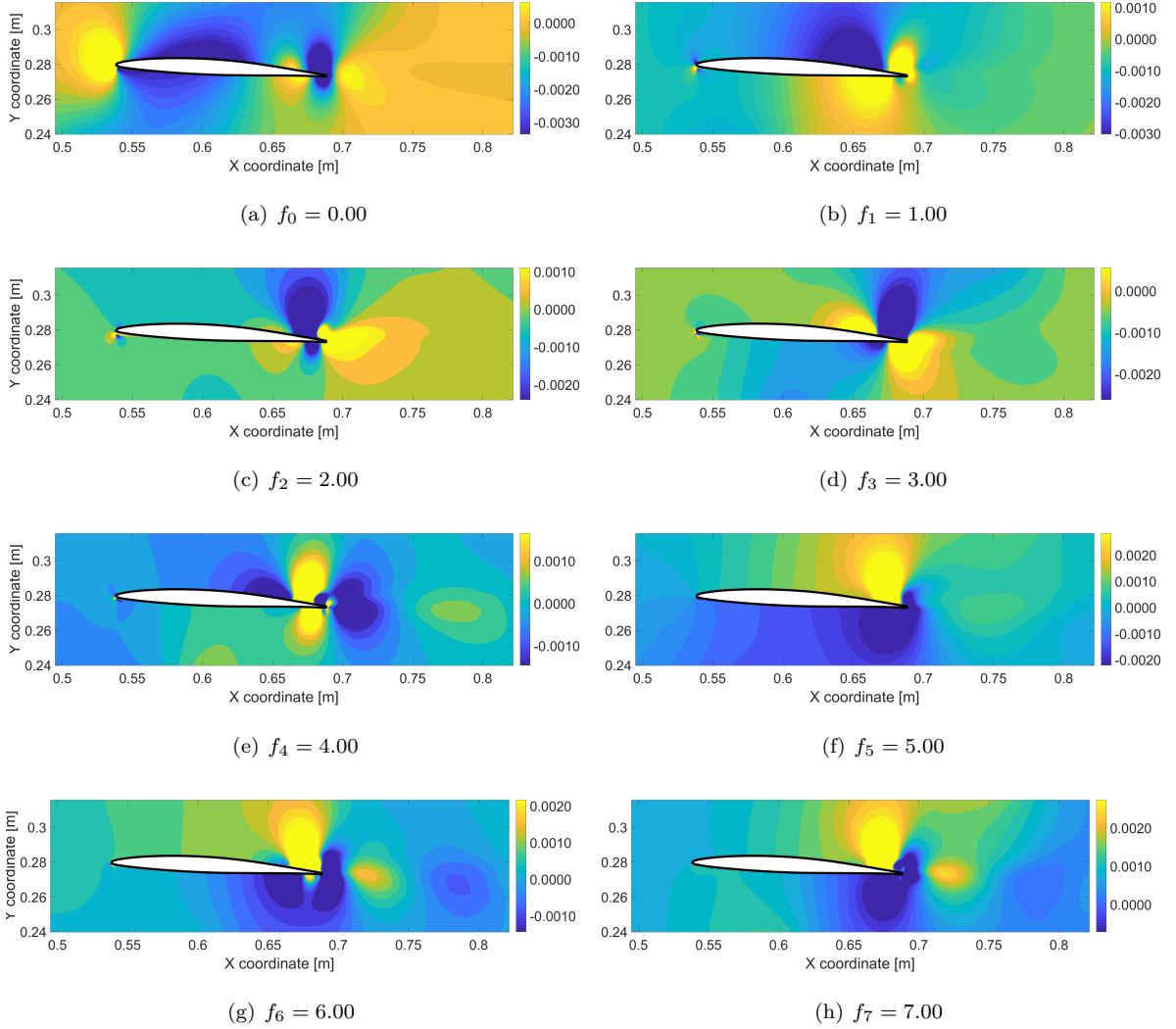
14

Figure 7: DMD modes of pressure field with different normalized frequencys ($f_n = \frac{f}{f_{osc}}$ with $f_{osc} = 19.17$Hz; $n = 0, 1, 2, 3...$) on the central blade; plasma on; IBPA = -51°.

amplitudes for all modes except mode 1 (compare, e.g., mode 4 in figures 6(d) and 7(d)). This higher amplitude variation is especially, but not solely, located close to the actuation area.

The DMD mode at the fundamental oscillation frequency for the actuated case also provides insight regarding the circulation effects close to the trailing edge. As clearly seen in figure 7(b), the yellow SS pressure lobe is extended downstream past the trailing edge. These modal features are also observed for all other IBPAs simulated, not shown here for

brevity. Such extension of the SS influence area is consistent with previous observations by the authors, reported as a downstream shift of the Kutta condition [33, 34]. This is due to the vortical structures generated by PS/SS actuation, which enable a finite non-zero pressure difference also in the area immediately downstream the trailing edge. At the trailing edge, the high pressure "protrusion" from the SS to the PS shows that acceleration induced by PS upstream actuation draws down the flow from the SS, consistent with the results of Choi [35].

Another interesting fact are the peaks of positive and negative pressure close to the leading edge. These can be seen at the fundamental frequency (and its first integer multiples) in figures 6 and 7. The large pressure gradients close to the leading edge promote a periodic oscillation of the stagnation point. This fluctuation influences the pressure field adjacently, yielding the observed modal decompositions.

The previous DMD modal results point out that the flow dynamics in the present simulations are determined mostly by three factors: i) for the clean and actuated cases, the cascade travelling waves seem to influence the whole passage between blades; ii) the oscillating blades promote a periodic swing of the stagnation point and the pressure gradients close to the leading edge, with effects observable in the non-zero frequency DMD modes; iii) for the actuated cases especially, a clear actuation footprint is seen close to the actuators, in comparison to the clean case. Moreover, a change in "effective camber" (or shift in the Kutta condition) is also portrayed in the DMD modes.

4.2. Singular value and modal coherence

The DMD singular values and the modal coherence metric discussed in Section 3 are here analysed. Figure 8 shows the discrete-system eigenvalue ω distribution for IBPA = -51°, for both clean and actuated cases (corresponding to figures 6 and 7, respectively). The horizontal axis shows the real part of the continuous eigenvalue ($\Re(\omega)$), while the vertical axis shows the normalized DMD mode frequency (directly proportional to $\Im(\omega)$). Again the oscillation frequency is used for normalization. Higher-frequency modes are not shown for clarity. The size and colour of each mode represents the modal coherence previously discussed. The dotted grey lines correspond to the fundamental oscillation frequency and its harmonics. A perfect symmetry is seen with respect to the null frequency. This happens

because the analysed data is purely real, by construction; therefore no new information is obtained by analysing the negative-frequency modes [32].
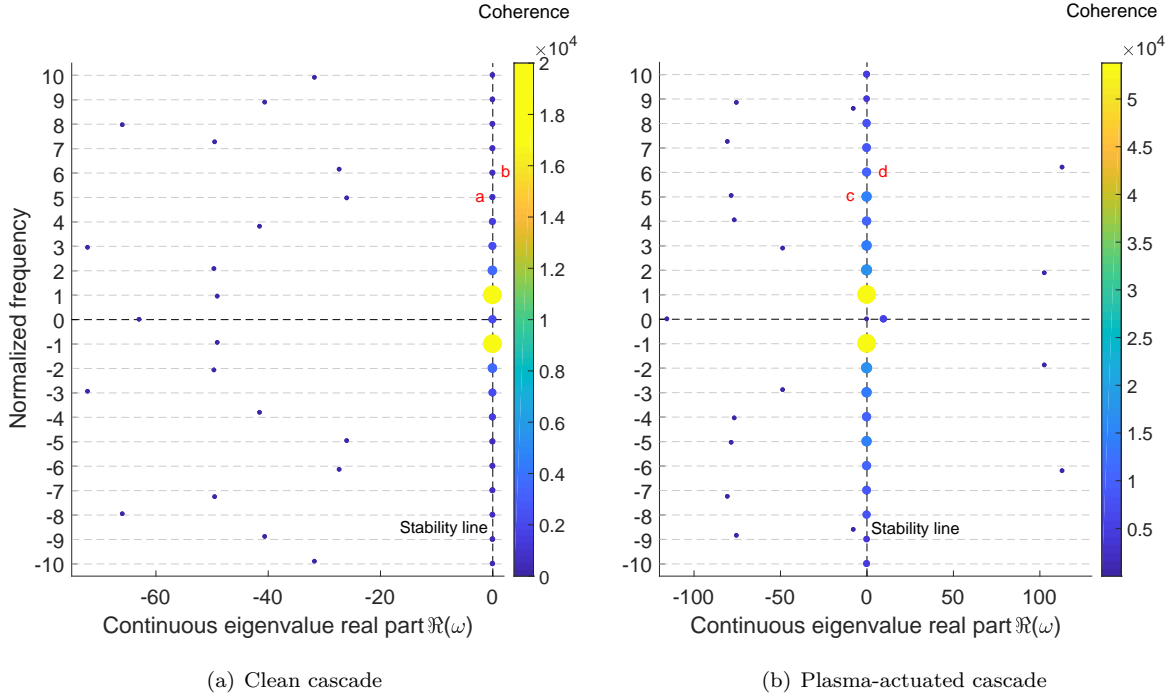

(a) Clean cascade (b) Plasma-actuated cascade

Figure 8: Continuous eigenvalue distribution for IBPA = -51°. Marker size and colour scale show the coherence metric for each DMD mode. The dotted grey lines correspond to the fundamental oscillation frequency and its harmonics. Remark: only low-frequency modes shown here.

Initially, one notices that the DMD modes are uniformly distributed at the multiples of the fundamental oscillation/actuation frequency of 19.17 Hz. Secondly, for the clean cascade (figure 8(a)), particularly the first oscillating mode (shown in figure 6(b)) conveys the most coherence, while a sharp decay is observed for the higher harmonics; the actuated case (figure 8(b)) depicts on the other hand a much slower decay of coherence along the first oscillating modes. Comparing e.g. the DMD modes with the 5th and 6st fundamental frequency in figure 8, it is clearly seen that the modes for the clean case, which are labelled with a and b, already have a much lower coherence level than the modes for the actuated case, which are labelled with c and d. This slower modal decay can also be inferred from the spatial modes. The contrast between the high coherence modes (top row of figure 6) and the low coherence modes (bottom row) indicates that the most relevant information in the clean case is contained in the mean flow and the first oscillating mode, whereas

17

higher-order modes do not help pinpointing large-scale coherent flow structures. On the other hand, figure 7 illustrates a broad spread in information into higher order modes for the actuated case. This conclusion can also be inferred from the magnitude of the DMD modes, shown in the scales of figures 6 and 7: low-coherence modes present a much smaller pressure footprint than the high-coherence counterpart.

To clearly indicate this contrast in coherence decay, figure 9 displays the modal coherence as a function of DMD normalized frequency for the aforementioned clean and actuated cases with IBPA = -51°, in a logarithmic scale. A smoother decay takes place for the clean cascade, while a slower and discontinuous decay is observed for the actuated counterpart. Comparing each mode in both curves, the coherence for the actuated case is always higher. Portraying this decay in coherence is comparable to showing a decay in the modal energy for a proper orthogonal decomposition, in the sense that the first modes with more coherence (energy) describe the most meaningful flow structures in the data. Similar results are obtained for other IBPAs, not shown here for brevity. This coherence disparity between clean and actuated cases substantiates that the plasma manages to dominate the cascade instabilities (originally driven by the travelling wave in the clean setup).

A few comments should be drawn regarding the eigenvalue stability analyses. For the clean case depicted in figure 8(a), near the fundamental frequency and harmonics, a pair of two DMD modes appear, one mode having a significant higher coherence and laying very close to the stability line. The latter attribute implies that the flow features represented by the DMD - modes have a very periodic characteristic. The modes laying on the left side of the stability line yield very stable eigenvalues ($\Re(\omega) \ll 0$), and do not play the most significant role in an eventual DMD field reconstruction. For the actuated case depicted in figure 8(b) there also exist for each harmonic of the fundamental frequency a DMD - mode laying close to the stability line. These modes feature a much higher coherence and play the most significant role in an eventual DMD field reconstruction. Once more, other IBPAs yield analogous results, not shown here for succinctness.

4.3. Modes in the far-field

Up to now, the depiction of the DMD modes was concentrated in the blade neighbourhood, even though the entire cascade domain for the middle blade (see figure 1) was used as
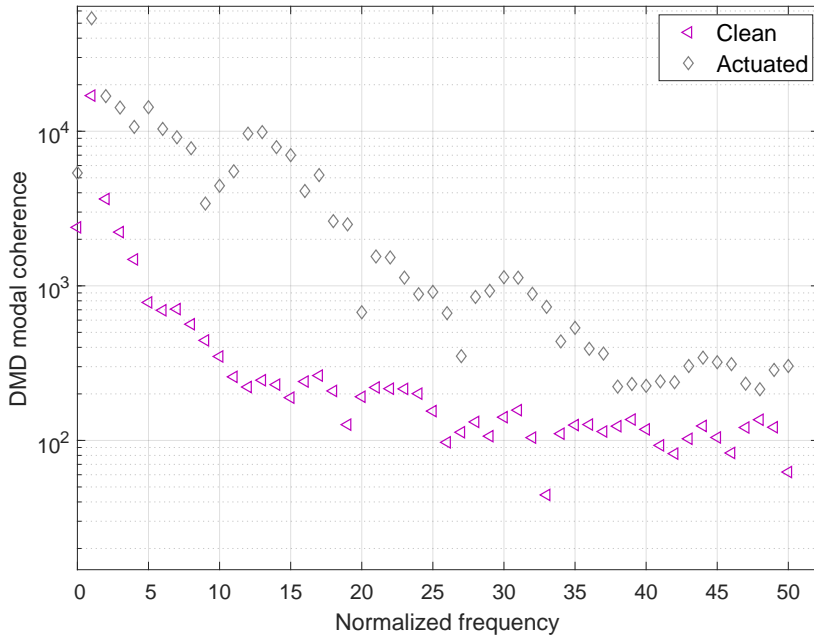
Figure 9: Modal coherence as a function of DMD frequency for IBPA = -51°. Clean and plasma-actuated cases are shown, corresponding to figure 8.

DMD data support. The impact of actuation on downstream rows lies outside the purpose of this manuscript and will be thoroughly assessed in future investigations. Nevertheless, a few remarks are made here about the downstream behaviour of the DMD modes.

High-order DMD modes are shown in figure 10, for the actuated case with IBPA = -90°. The two modes shown correspond to the 19th and 20th oscillation/actuation harmonics, displaying typical DMD downstream structures, asymmetrical and symmetrical with respect to the chord line, respectively. Similar modal flow structures have already been reported in several works, e.g.: [36, 37, 38] for numerical incompressible 2D cylinder flow; [31] for experimental shallow flow; [39] for the flow structures in the wake of a high-speed train; or [29] for the wake of a NACA airfoil equipped with a Gurney flap. In this work, however, these flow structures are strongly linked to the alternating actuation. Indeed, on clean configuration, the fast decay in the DMD coherence decreases the importance of high-order modes.

The DMD modes shown in figure 10 are directly linked to the blade oscillation and actuation frequency. Since the frequency is the same fundamental value for both phenomena -- the
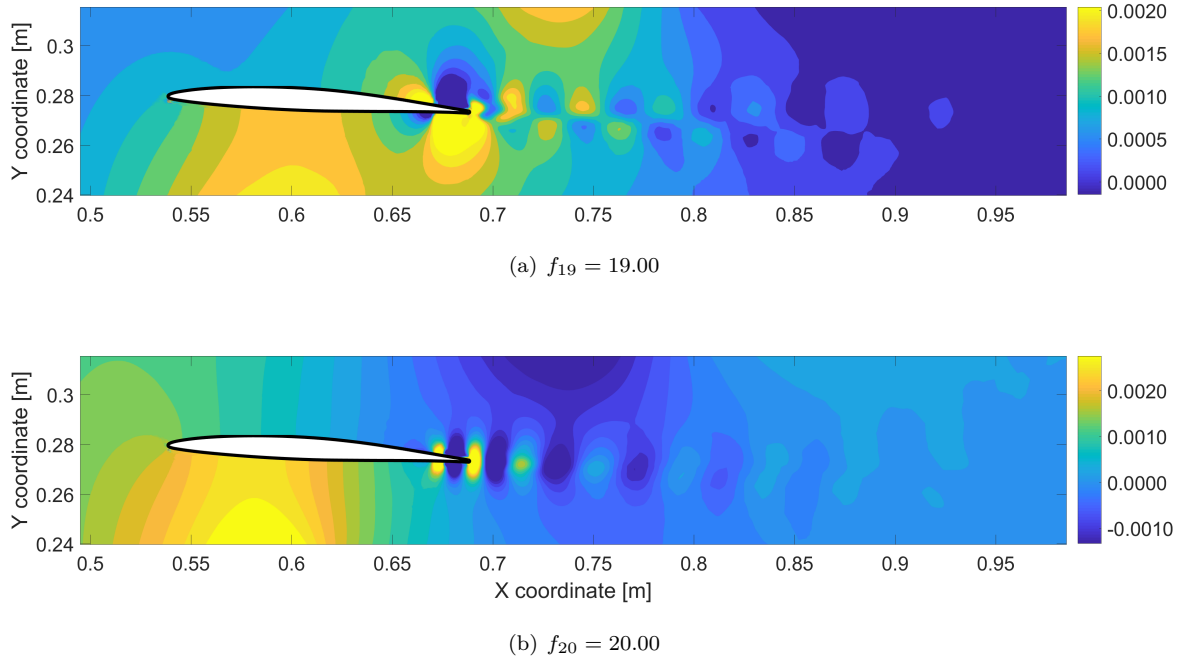
(a) $f_{19} = 19.00$

(b) $f_{20} = 20.00$

Figure 10: DMD modes of pressure field with different normalized frequencys ($f_n = \frac{f}{f_{osc}}$ with $f_{osc} = 19.17$Hz; $n = 0, 1, 2, 3...$) on the central blade with plasma on; IBPA = -90°.

actuation frequency is an integer multiple of the oscillation frequency -- the resultant modes carry effects related to both the oscillation and the plasma actuation. The modal-pressure magnitude decay downstream of the blades can be clearly noticed in the depicted high-order modes. The wake represented by these modes is dynamically weakened as it travels downstream. Considering each convecting pressure lobe of figure 10(a), about one chord downstream the trailing edge, the local amplitude is approximately 5 % of the values close to the actuation. For figure 10(b) a similiar fast decay can be seen: for this case the local amplitudes value decrease to about 8 % at one chord downstream.

Similar results are obtained for other IBPAs. A detailed assessment with more rows, including rotor and stator, would be necessary to proper evaluate the quantitative impact on downstream rows. However, the current results show that the positive stability effects obtained with the use of plasma actuation do not lead to extensive and long-lasting pressure fluctuations in the downstream field. Therefore, no relevant actuation-related disturbance effects in the downstream rows are foreseen.

5. Conclusions

Dynamic mode decomposition (DMD) is applied to the unsteady pressure field generated by a linear compressor cascade oscillating according to travelling wave pitching setups. Results from computational fluid dynamic simulations are used as a reference for the decomposition. The central blades of the cascade are equipped with pairs of trailing edge plasma actuators located on the pressure side and on the suction side. Alternate triggering of actuators on both sides allows to enhance remarkably the aeroelastic stability of the cascade.

The spatial pressure distributions issued by the dynamic mode decomposition show that the actuation causes relevant pressure alterations at the trailing edge and adjacently. Furthermore, the actuation influences the overall pressure modes in the fundamental frequency and its multiples, while no additional periodic event seems to occur. Another effect observed for all the considered spatial modes is the increase in flow energy due to actuation. Indeed, the actuated cases demand the analyses of more DMD modes compared to the clean cases, quite independently of the inter blade phase angle. The shift of the Kutta condition downstream the trailing edge observed in previous work is also clearly portrayed by the DMD modes.

The modal coherence also depicts the energy spread related to the actuation. For the clean cascade, the coherence decays by one order of magnitude for the 4th mode, when compared to the most coherent. For the actuated case, each mode yields not only more modal coherence (in direct comparison with the clean counterpart), but also the singular value decay is further spread in the spectrum.

Additionally, it is found that the flow dynamics can be correctly reproduced by a small number of modes, without the need of involving the high frequency small spatial scale dynamics computed by numerical simulations. The advantages of the applied decomposition are twofold. On one hand, the projection of the flow dynamics into a space with a reduced number of degrees of freedom enables to perform large-scale optimization studies for the actuation law, without recurring to time and resource-consuming numerical simulations. On the other hand, the DMD allows for getting an insight into the most relevant flow patterns. Therefore, the applied dynamic mode decomposition can be successfully used

for performing large scale optimization studies on the actuation parameters and in turn maximize the benefits of plasma actuation for aeroelastic control on turbomachinery blades.

Acknowledgements

References

[1] C. Tiedemann, A. Heinrich, and D. Peitsch. A New Linear High Speed Compressor Stator Cascade for Active Flow Control Investigations. In *6th AIAA Flow Control Conference*, number AIAA 2012-3251, New Orleans, LA, USA, 2012.

[2] M. Matejka, L. Popelka, P. Safarik, and J. Nozicka. Influence of Active Methods of Flow Control on Compressor Blade Cascade Flow. In *ASME Turbo Expo, 9--13 June 2008, Berlin, Germany*, number GT2008-51109, 2008.

[3] Z. Trávníček, V. Cyrus, D. Šimurda, M. Luxa, J. Lukač, and J. Kordik. Experimental investigation of the compressor cascade under an active flow control. *EPJ Web of Conferences*, 45, 2013.

[4] S. Hammer, D. T. Phan, J. Peter, T. Werder, R. Meyer, R. Liebich, and P. U Thamsen. Active flow control by adaptive blade systems in periodic unsteady flow conditions. In *Active Flow and Combustion Control*, Berlin, Germany, 2014.

[5] H. P. Monner, O. Huxdorf, J. Riemenschneider, and R. Keimer. Design and manufacturing of morphing fan blades for experimental investigations in a cascaded wind tunnel. In *23rd AIAA/AHS Adaptive Structures Conference, 5--9 January 2015, Kissimmee, FL, USA*, number AIAA 2015-0790, Kissimmee, FL, USA, 2015. American Institute of Aeronautics and Astronautics.

[6] D. T. Phan, P. Springer, and R. Liebich. Numerical investigation of an elastomer-piezo-adaptive blade for active flow control of a nonsteady flow field using fluid-structure interaction simulations. *Journal of Turbomachinery*, 139:091004--1--091004--10, 2017.

[7] M. G. De Giorgi, E. Pescini, F. Marra, and A. Ficarella. Experimental and numerical analysis of a micro plasma actuator for active flow control in turbomachinery. In *Proceedings of ASME Turbo Expo 2014:*

Turbine Technical Conference and Exposition, number GT2014-25337, Düsseldorf, Germany, 2014. American Society of Mechanical Engineers.

[8] V. Motta, L. Malzacher, P. Neumann, and D. Peitsch. Numerical assessment of virtual control surfaces for compressor blades. In *AIAA Aviation Forum*, number AIAA 2017-3909, Denver, COL, USA, 2017. American Institute of Aeronautics and Astronautics.

[9] V Motta, L Malzacher, and D Peitsch. Numerical assessment of virtual control surfaces for load alleviation on compressor blades. *Applied Sciences, special issue on Active Flow Control Technologies for Energy and Propulsive Systems*, 8(125):1--22, 2018.

[10] V. Motta, L. Malzacher, and D. Peitsch. Numerical investigation of virtual control surfaces for vibration control on compressor blades. In *International Forum on Aeroelasticity and Structural Dynamics*, number IFASD-137, Como, Italy, 2017.

[11] V. Motta, L. Malzacher, and D. Peitsch. Numerical investigation of virtual control surfaces for aeroelastic control on compressor blades. *Journal of Fluids and Structures*, 81:617--637, 2018.

[12] J. Belz, M. May, J. Siemann, J. R. Seume, C. Voigt, H. Böhmer, and B. Grüber. Excited blade vibration for aeroelastic investigations of a rotating blisk using piezo-electric macro fiber composites. In *ASME Turbo Expo 2013: Turbine Technical Conference and Exposition*, number GT2013-95735, San Antonio, Texas, USA, 2013.

[13] X. Q. Huang and D. L. Bell. Influence of upstream stator on rotor flutter stability in a low pressure steam turbine stage. *Proceedings of the Institution of Mechanical Engineers, Part A: Journal of Power and Energy*, 220(2):23--35, 2006.

[14] S. Saddoughi, G. Bennett, M. Boespflug, S. L. Puterbaugh, and A. R. Wadia. Experimental investigation of tip clearance flow in a transonic compressor with and without plasma actuators. *Journal of Turbomachinery*, 137(4):041008, 2014.

[15] P. J. Schmid. Dynamic mode decomposition of numerical and experimental data. *Journal of Fluid Mechanics*, 656:5--28, 2010.

[16] L. Malzacher, S. Geist, D. Peitsch, and H. Hennings. A low speed compressor test rig for flutter investigations. In *Proceedings of ASME Turbo Expo 2016: Turbomachinery Technical Conference and Exposition*, number GT2016-57960, Seoul, South Korea, 2016.

[17] M. C. Keerthi, S. Shubham, and A. Kushari. Aerodynamic Influence of Oscillating Adjacent Airfoils in a Linear Compressor Cascade. *AIAA Journal*, 55(12):4113--4126, 2017.

[18] E. Akcayoz, D. V. Huu, and A. Mahallati. Controlling corner stall separation with plasma actuators in a compressor cascade. *Journal of Turbomachinery*, 138(8):081008--1--081008--13, 2016.

[19] T. C. Corke, M. L. Post, and D. M. Orlov. SDBD plasma enhanced aerodynamics: Concepts, Optimization and Applications. *Progress in Aerospace Sciences*, 43(7--8):193--217, 2007.

[20] H. Zhang, X. Yu, B. Liu, Y. Wu, and Y. Li. Control of corner separation with plasma actuation in a high-speed compressor cascade. *Applied Sciences*, 7(5):465--480, 2017.

[21] V. Motta, A. Zanotti, G. Gibertini, and G. Quaranta. Numerical assessment of an L-shaped Gurney flap for load control. *Proceedings of the Institution of Mechanical Engineers, Part G: Journal of Aerospace Engineering*, 231(5):951--975, 2016.

[22] F. Lane. System mode shapes in the flutter of compressor blade rows. *Journal of the Aeronautical Sciences*, 23(1):54--66, 1956.

[23] W. Sachs. Windkanal für instationäre Gitter (WiG), Messstrecke für instationäre Gitter (MiG). Phase 1: Bau und Inbetriebnahme Windkanal für instationäre Gitter (WiG). Technical report 232-90, DLR, 1990.

[24] A. Zanotti, D. Grassi, and G. Gibertini. Experimental investigation of a trailing edge L-shaped tab on a pitching airfoil in deep dynamic stall conditions. *Proceedings of the Institution of Mechanical Engineers, Part G: Journal of Aerospace Engineering*, 228(12):2371--2382, 2014.

[25] G. Berkooz, P. Holmes, and J.L. Lumley. The proper orthogonal decomposition in the analysis of turbulent flows. *Annual Review of Fluid Mechanics*, 25(1):539--575, 2011.

[26] Q. Zhang, Y. Liu, and S. Wang. The identification of coherent structures using proper orthogonal decomposition and dynamic mode decomposition. *Journal of Fluids and Structures*, 49:53--72, 2014.

[27] G. Jodin, V. Motta, J. Scheller, E. Duhayon, C. Döll, J-F. Rouchon, and M. Braza. Dynamics of a hybrid morphing wing with active open loop vibrating trailing edge by time-resolved PIV and force measures. *Journal of Fluids and Structures*, (74):263--290, 2017.

[28] C. W. Rowley, I. Mezić, S. Bagheri, P. Schlatter, and D. S. Hanningson. Spectral analysis of nonlinear flows. *Journal of Fluid Mechanics*, 641:115--127, 2009.

[29] C. Pan, D. Yu, and J. Wang. Dynamical mode decomposition of gurney flap wake flow. *Theoretical and Applied Mechanics Letters*, 1(1):012002, 2011.

[30] A. Seena and H. J. Sung. Dynamic mode decomposition of turbulent cavity flows for self-sustained oscillations. *International Journal of Heat and Fluid Flow*, 32:1098--1110, 2011.

[31] J.E. Higham, W. Brevis, and C.J. Keylock. Implications of the selection of a particular modal decomposition technique for the analysis of shallow flows. *Journal of Hydraulic Research*, 56(6):796--805, 2018.

[32] P. J. Schmid, L. Li, M. P. Juniper, and O. Pust. Applications of the dynamic mode decomposition. *Theoretical and Computational Fluid Dynamics*, 25(1-4):249--259, 2010.

[33] V. Motta, L. Malzacher, V. B. C. de Almeida, T. D. Phan, R. Liebich, D. Peitsch, and G. Quaranta. A physically consistent reduced order model for plasma aeroelastic control on compressor blades. *Journal of Engineering for Gas Turbines and Power*, (GTP-19-1090), 2019.

[34] V. Motta, L. Malzacher, V. B. C. de Almeida, and D. Peitsch. Aeroelastic control on compressor blades with virtual control surfaces: A numerical assessment. In *Proceedings of ASME Turbo Expo 2018, Volume 7C: Structures and Dynamics*, number GT2018-75079, Oslo, Norway, 2018. ASME.

[35] L. Feng, K. Choi, and J. Wang. Flow control over an airfoil using virtual Gurney flaps. *Journal of Fluid Mechanics*, 767:595--626, 2015.

[36] J. Kutz. *Dynamic mode decomposition : data-driven modeling of complex systems*. Society for Industrial and Applied Mathematics, Philadelphia, 2016.

[37] J. N. Kutz, S. L. Brunton, D. M. Luchtenburg, C. W. Rowley, and J. H. Tu. On dynamic mode decomposition: Theory and applications. *Journal of Computational Dynamics*, 1(2):391--421, 2014.

[38] K. K. Chen, J. H. Tu, and C. W. Rowley. Variants of dynamic mode decomposition: Boundary condition, koopman, and fourier analyses. *Journal of Nonlinear Science*, 22(6):887--915, 2012.

[39] T. W. Muld, G. Efraimsson, and D. S. Henningson. Flow structures around a high-speed train extracted using proper orthogonal decomposition and dynamic mode decomposition. *Computers & Fluids*, 57:87--97, 2012.